Time-dependent density functional theory calculations of the spectroscopy of core electrons

Nicholas A. Besley* and Frans A. Asmuruf

Received 2nd February 2010, Accepted 21st June 2010
DOI: 10.1039/c002207a

Recent advances in X-ray sources have led to a renaissance in spectroscopic techniques in the X-ray region. These techniques that involve the excitation of core electrons can provide an atom specific probe of electronic structure and provide powerful analytical tools that are used in many fields of research. Theoretical calculations can often play an important role in the analysis and interpretation of experimental spectra. In this perspective, we review recent developments in quantum chemical calculations of X-ray absorption spectra, focusing on the use of time-dependent density functional theory to study core excitations. The practical application of these calculations is illustrated with examples drawn from surface science and bioinorganic chemistry, and the application of these methods to study X-ray emission spectroscopy is explored.

I. Introduction

While less familiar than analogous techniques for valence electrons, studying and exploiting the spectroscopy of core electrons has a long history.[1] The spectroscopy of core electrons is attractive for several reasons. The spatially local nature of the core orbitals and large energy difference between the core orbitals of different elements means that the spectroscopic techniques can provide an atom specific probe of electronic structure. A drawback of these techniques is the high energy X-ray light source required, and this has hindered the wide spread use of core-electron spectroscopic methods. However, in recent years there has been considerable advances in the quality and availability of X-ray sources. In particular, new synchrotron sources provide much greater intensity and resolution, and this has provided spectroscopy in the X-ray region with a richness in structure that can match more traditional spectroscopy in the ultraviolet region.

There are a number of commonly used X-ray spectroscopic techniques. Fig. 1 shows a schematic of an absorption spectrum in the X-ray region. The structure near the absorption edge is referred to as near edge X-ray absorption fine structure (NEXAFS) or X-ray absorption near edge structure (XANES) and corresponds to the excitation of a core electron to give a bound state below the ionization continuum. This part of the X-ray absorption spectrum provides information on the unoccupied orbitals. At higher energy, usually beyond 20–30 eV of the absorption edge, are weak oscillations which correspond to extended X-ray absorption fine structure (EXAFS) and arise from excitation to states above the ionization continuum and subsequent scattering of the photoelectron by its environment. For some systems, pre-edge features are observed that arise from

School of Chemistry, University of Nottingham, University Park, Nottingham NG7 2RD, UK. E-mail: nick.besley@nottingham.ac.uk

Nicholas A. Besley

Dr Nick Besley studied Chemical Physics at the University of Sussex, and obtained a PhD in 1997 from the University of Birmingham, under the supervision of Professor Peter Knowles. He spent the following two years as a postdoctoral research associate at The Scripps Research Institute in California. He returned to the UK in 1999 to work as a postdoctoral fellow at the University of Nottingham with Professor Peter Gill. In 2002 he was awarded an EPSRC Advanced Research Fellowship and was subsequently appointed as a Lecturer in Theoretical Chemistry at Nottingham in 2005. His research is focused on computing the spectroscopy of large molecules.

Frans A. Asmuruf

Frans Asmuruf obtained a BSc degree from the University of Cenderawasih (Papua) and a MSc degree in Physical Chemistry from the Bandung Institute of Technology (Indonesia). Subsequently, he was appointed as a Junior Lecturer in the Department of Chemistry, University of Cenderawasih. In 2005 Frans was awarded a Scholarship of the Papua Government to undertake research toward a PhD degree, and he is currently completing his PhD thesis on quantum chemical calculations of core electron spectroscopies at the University of Nottingham, UK.

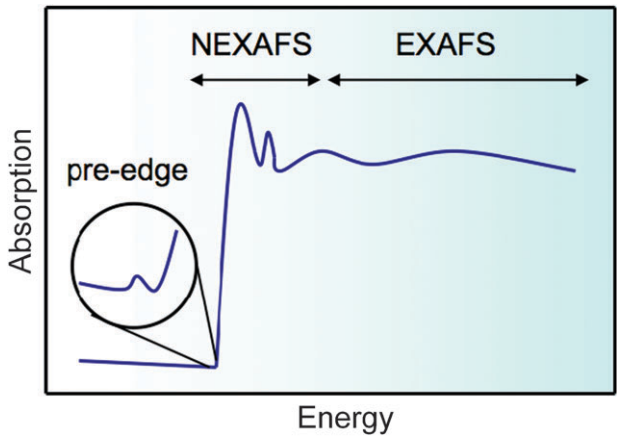

Fig. 1 Schematic of a X-ray absorption spectrum.

excitation from the core orbitals to singly occupied orbitals. In addition to these absorption processes, X-ray emission can also occur. Excitation of a core electron creates a singly occupied core orbital, referred to as a core hole. X-ray emission spectroscopy (XES) results from the subsequent decay of a valence electron to the vacant core orbital with the emission of a photon. XES is dependent on the nature of the occupied valence orbitals, and thus provides complementary information to NEXAFS. Another related technique is Auger spectroscopy. This also arises from the decay of a valence electron to a core hole, but in Auger spectroscopy the excess energy results in the emission of an electron.

Surface science is a field of research that has exploited X-ray spectroscopy extensively, providing information on the structure and orientation of adsorbed molecules and the nature of the bonding to the surface.[1,2] However, X-ray spectroscopic techniques are used in a wide variety of applications, including bioinorganic chemistry,[3–5] thin films[6] and recent high profile experiments probing the structure of water,[7,8] and in the future it is likely that this range of applications will grow. In comparison to the vast literature concerned with the calculation of excited states following the excitation of valence electrons, the number of studies focusing on the calculation of core-excited states is modest. However, such calculations can play a crucial role in aiding the interpretation and understanding of experimental spectra, and the development of accurate calculations remains important to future progress in the application of X-ray spectroscopic methods. In this perspective, we review recent developments in time-dependent density functional theory (TDDFT) calculations of NEXAFS, and illustrate how they can inform the interpretation of experiment with applications drawn from surface science and bioinorganic chemistry, and the extension of these methods to study X-ray emission spectroscopy is explored.

II. Calculations of near edge X-ray absorption fine structure

There are several theoretical approaches to computing NEXAFS spectra. Many early calculations used the multiple scattering X_α method.[1] This approach has proved successful in the EXAFS region, but the muffin-tin approximation in the method has made it less satisfactory in the NEXAFS region and led to the development of alternative approaches. One such method is the direct static exchange (STEX) method.[9–11] In this independent channel single electron approach the contribution to the molecular potential of the excited electron is neglected. The calculation of the absorption spectrum comprises a number of steps. A calculation of the core–hole state is performed with the valence orbitals frozen, followed by optimization of the valence orbitals with the core hole frozen. The STEX Hamiltonian is diagonalized and the excitation energies are obtained by summing the core ionization potential to the eigenvalues of the STEX Hamiltonian. The oscillator strengths are calculated from the dipole matrix elements between the ground and the final STEX states. The limitations of this approach are the neglect of electron correlation and the independent channel approximation. In an effort to improve the STEX approach, the transition potential method was introduced.[12,13] In this approach, the orbital binding energy is computed as the derivative of the total energy with respect to the orbital occupation number. To take into account the relaxation of the orbitals, the energy is approximated by calculating the derivative at the point corresponding to the occupation 0.5. Formally, this corresponds to a core orbital with half an electron removed which captures a balance between final and initial states. However, the procedure can be performed with different fractional occupancies such as 0.0 which corresponds to a full core hole.[14] The transition potential method has proved successful and has been applied to a wide variety of problems. The excitation energies obtained from the transition potential method are about 1.5–2 eV too low, and this error has been attributed to higher order contributions to the core relaxation energies.[13] Standard quasi-particle theory has also been developed to study core X-ray absorption spectra.[15] An advantage of this approach is that it is able to treat NEXAFS and EXAFS within a common framework. Better agreement with experiment is found at higher energies, while discrepancies close to the absorption edge illustrate that modifications to the quasi-particle theory are required.[15] An equations of motion coupled cluster (EOM-CCSD) based approach has been shown to provide accurate core excitation energies.[16] This approach uses a two step procedure, firstly, a CCSD calculation on the core ionized state is performed to describe the relaxation of the core ion. Subsequently, an electron is added to the core ionized state using the electron attachment EOM-CCSD method to obtain the core-excited states of the neutral molecule. The symmetry-adapted-cluster configuration interaction (SAC-CI) method has also been applied to study X-ray absorption spectroscopy.[17–21] The focus of these studies has been the study of satellite peaks and the analysis and simulation of vibrational structure.

In recent years, there has been many advances in density functional theory (DFT) and this perspective is primarily concerned with the the application and development of these methods for the study of core excitations and X-ray absorption spectra in the region close to the absorption edge. Within DFT, a ΔKohn–Sham method is the most intuitively simple approach to computing NEXAFS spectra. In a ΔKohn–Sham approach the core excitation energy is the

difference in the expectation values of the neutral and core-excited Kohn–Sham Hamiltonians, where the orbitals have been variationally optimized for the different states. However, obtaining a core-excited state with a Kohn–Sham formalism is not straightforward, and usually some constraints, overlap criterion or intermediate optimization with a frozen core hole is used to prevent the collapse of the core hole during the self-consistent field (SCF) procedure.[22–24] We use an overlap approach to finding excited state solutions of the SCF equations termed the maximum overlap method (MOM).[25] On an iteration within a SCF procedure the Kohn–Sham matrix is formed from the current molecular orbitals. Solving the generalised eigenvalue problem

$$\mathbf{F}\mathbf{C}^{\mathrm{new}} = \mathbf{S}\mathbf{C}^{\mathrm{new}}\boldsymbol{\varepsilon} \quad (1)$$

(where **S** is the basis function overlap matrix) gives the new molecular orbital coefficient matrix $\mathbf{C}^{\mathrm{new}}$ and orbital energies $\boldsymbol{\varepsilon}$. In conventional approaches, the n orbitals with the lowest orbital energies are then occupied. However, excited state solutions can be obtained by defining an alternative set of occupied orbitals. For example, for core-excited states a single occupancy of a core orbital can be maintained throughout the SCF process, and the relevant core orbital can be identified by the overlap between the new and old set of orbitals.[22] In the maximum overlap method, the orbitals that are occupied are chosen to be those that overlap most with the *span* of the old occupied orbitals. The new occupied orbitals are identified by defining an orbital overlap matrix

$$\mathbf{O} = (\mathbf{C}^{\mathrm{old}})^{\dagger}\mathbf{S}\mathbf{C}^{\mathrm{new}} \quad (2)$$

O_{ij} gives the overlap between the ith old orbital and the jth new orbital and the projection of the jth new orbital onto the old occupied space is

$$p_j = \sum_{i}^{n} O_{ij}^2 \quad (3)$$

where

$$O_{ij} = \sum_{\nu}^{N}\left[\sum_{\mu}^{N} C_{i\mu}^{\mathrm{old}} S_{\mu\nu}\right] C_{\nu j}^{\mathrm{new}} \quad (4)$$

The n occupied orbitals are chosen to be the ones with the largest projections p_j. This approach is applicable in non-symmetric systems in which there is a significant difference between the old and new set of orbitals. An advantage of the ΔKohn–Sham approach is that the relaxation of the core hole is included, and a recent study showed that core excitation energies computed with the B3LYP functional were in good agreement with experiment, provided uncontracted basis functions were used.[26]

The principal disadvantage of the ΔKohn–Sham approach is that a separate calculation is required for each core-excited state. Computing NEXAFS spectra for even relatively small molecular systems requires many different core-excited states to be computed, and the calculations can become expensive and tedious. Consequently, TDDFT in which the excited states are obtained within a single calculation becomes an attractive option for computing NEXAFS spectra. TDDFT is well established for computing valence excited states and is described in detail elsewhere.[27] Within the Tamm–Dancoff approximation[28] of TDDFT, excitation energies and oscillator strengths are determined as the solutions to the eigenvalue equation[27]

$$\mathbf{A}\mathbf{X} = \omega\mathbf{X} \quad (5)$$

The matrix **A** is given by

$$\mathrm{A}_{ia\sigma,jb\tau} = \delta_{ij}\delta_{ab}\delta_{\sigma\tau}(\varepsilon_{a\sigma} - \varepsilon_{i\tau}) + (ia\sigma|jb\tau) + (ia\sigma|f_{XC}|jb\tau) \quad (6)$$

where

$$(ia\sigma|jb\tau) = \iint \psi_{i\sigma}^{*}(\mathbf{r}_1)\psi_{a\sigma}^{*}(\mathbf{r}_1)\frac{1}{r_{12}}\psi_{j\tau}(\mathbf{r}_2)\psi_{b\tau}(\mathbf{r}_2)\mathrm{d}\mathbf{r}_1\mathrm{d}\mathbf{r}_2 \quad (7)$$

$$(ia\sigma|f_{XC}|jb\tau) = \int \psi_{i\sigma}^{*}(\mathbf{r}_1)\psi_{a\sigma}(\mathbf{r}_1)\frac{\partial^2 E_{\mathrm{XC}}}{\partial\rho_{\sigma}(\mathbf{r}_1)\partial\rho_{\tau}(\mathbf{r}_2)} \times \psi_{j\tau}(\mathbf{r}_2)\psi_{b\tau}^{*}(\mathbf{r}_2)\mathrm{d}\mathbf{r}_1\mathrm{d}\mathbf{r}_2 \quad (8)$$

and ε_i are the orbital energies and E_{XC} is the exchange correlation functional. Within standard implementations of TDDFT, the calculation of core-excited states becomes prohibitively expensive due to the large number of roots required to obtain the high energy core-excited states. Stener and co-workers[29] recognized that a practical solution to this problem is to restrict the single excitation space to include only excitations from the relevant core orbital(s), and subsequently other authors have exploited this approach.[30,31] This makes the calculation of core-excited states of comparable expense to computing valence excited states whilst introducing a negligible error. For small systems, the error can be evaluated directly by comparing the results from calculations with the truncation of the excitation space to analogous calculations with the full excitation space. For a range of core excitations from 1s orbitals, the largest error observed was 0.01 eV in the excitation energy and 0.01 in the oscillator strength.[32] Different approaches to computing core-excited states within TDDFT have also been reported. The Sakurai–Sugiura projection method can be used to find excitation energies in a specified range, and this has been implemented within TDDFT and shown to be an efficient approach for core excitations.[33] Alternatively, Norman and co-workers have used a resonant converged complex polarization propagator to study NEXAFS.[34,35] In general, these methods provide a spectral profile that agrees well with experimental measurements.

At the heart of these TDDFT calculations is the exchange–correlation functional, and the nature of this functional dictates the accuracy of the computed core excitation energies and NEXAFS spectra. Unfortunately, standard generalized gradient approximation and hybrid functionals fail dramatically for core excitations resulting in a large underestimation of the excitation energy. Furthermore, the extent of this underestimation increases with the charge of the nuclei on which the core orbitals are localized.[36] This failure stems from the approximate exchange within the exchange–correlation functionals and is associated with the self interaction error,[30,38–42] and self-interaction corrections have been explored to correct for this error.[40,41] There is an analogy between the calculation of core-excited states and the calculation of charge transfer states. The failure of TDDFT to

describe charge transfer states is well understood,[43] and can be predicted by the Λ diagnostic.[44] This diagnostic is a measure of the overlap between donating and accepting orbitals, and is given by

$$\Lambda = \frac{\sum_{i,a} \kappa_{ia}^2 o_{ia}}{\sum_{i,a} \kappa_{ia}^2} \quad (9)$$

where o_{ia} is a measure of the spatial overlap between occupied orbital ψ_i and virtual orbital ψ_a

$$o_{ia} = \int |\psi_i(\mathbf{r})||\psi_a(\mathbf{r})| d\mathbf{r} \quad (10)$$

and within the Tamm–Dancoff approximation

$$\kappa_{ia} = X_{ia}. \quad (11)$$

Table 1 shows computed values of Λ for a range of core excitation energies. The compactness of the core orbital makes the values of Λ small, and comfortably in the regime where generalized gradient approximation (GGA) or hybrid functionals fail.[44] For nuclei with higher nuclear charge, the core orbitals will be more compact and a greater failure of the functional would be anticipated. In general, this underestimation is roughly constant across different excitations from a given core orbital, and a pragmatic approach is to simply apply a constant shift to the computed spectra.[45,46] However, it remains desirable to compute accurate core excitations within TDDFT, and several groups have developed new exchange–correlation functionals designed for NEXAFS calculations.[30,37–39,47,48]

Nakai and co-workers reported the first attempts to improve the description of core-excited states within TDDFT. The BmLBLYP exchange–correlation functional[47] was developed from the observation that the modified Leeuwen–Baerends (mLB) exchange functional performed better for core excitations and Becke88 (B) exchange was better for valence excitations. The resulting functional combined these two exchange functionals by adopting LB94 in the core and asymptotic regions and Becke88 in the valence regions, and gave an average error of about 1.5 eV for a set of core excitations compared to over 13 eV for B3LYP. Subsequently, the CV-B3LYP[37] and CVR-B3LYP[38,39] functionals were introduced. These functionals were designed to be accurate for all types of excitation, including core excitations, and worked by using an appropriate fraction of HF exchange depending on the type of excitation. These functionals were applied to core-excitations from first and second row nuclei and showed a substantial improvement in accuracy, yielding mean absolute errors below 1 eV.

Table 1 Values of the Λ diagnostic for core excitations from BLYP/6-311(2+,2+)G** calculations

Excitation	Λ
CO C(1s) → π*	0.18
CO C(1s) →3s	0.04
CO O(1s) → π*	0.14
CO O(1s) →3s	0.03
HF F(1s) → σ*	0.08
SiH_4 Si(1s) → σ*	0.03
H_2S S(1s) → σ*	0.04
H_2S S(1s) →4p	0.01
HCl Cl(1s) → σ*	0.02
HCl Cl(1s) →$4p_\pi$	0.01

Following this work, we optimized a hybrid functional for carbon *K*-edge excitations which was used to study the NEXAFS spectroscopy of hydrocarbons adsorbed on the Si(100)-2×1 surface.[30] In this functional, the fraction of HF exchange in B3LYP was increased to predict the 1s → π* excitation energies in acetylene, ethylene and benzene correctly. This led to the following functional with 57% HF exchange, with the fraction of Becke exchange reduced proportionately

$$\mathrm{BH}^{0.57}\mathrm{LYP} = 0.57\mathrm{HF} + 0.35\mathrm{B} + 0.08\mathrm{S} + 0.81\mathrm{LYP} + 0.19\mathrm{VWN} \quad (12)$$

where HF, B and S are Hartree–Fock (HF), Becke[49] and Slater[50] exchange functionals, respectively, and LYP[51] and VWN[52] are correlation functionals. However, while this functional performs well for carbon *K*-edge excitations, its performance is less satisfactory for excitations for core excitations from other nuclei with a significantly different nuclear charge.

Building on the analogy with charge transfer excitations, Coulomb attenuated or range separated functionals have been developed for core excitations. These functionals exploit a partitioning of the $1/r_{12}$ operator in the evaluation of the exchange energy and have provided a solution to the charge transfer problem.[53–58] In these functionals, the long-range part of the exchange energy is evaluated primarily or completely using HF theory, and DFT exchange is primarily used for the short-range. However, such long-range corrected functionals developed for valence excitations do not improve core excitation energies, and the predicted values remain too low.[42,48] The first work in this area was reported by Hirao and co-workers who adapted the LCgau-DFT approach[59] to core excitations.[42] In traditional long-range corrected exchange functionals the $1/r_{12}$ operator is partitioned using the error function (erf) according to

$$\frac{1}{r_{12}} = \frac{\mathrm{erf}(\mu r_{12})}{r_{12}} + \frac{\mathrm{erfc}(\mu r_{12})}{r_{12}} \quad (13)$$

where $r_{12} = |\mathbf{r}_1 - \mathbf{r}_2|$ and erfc = 1 − erf.[53] The first term of eqn (13) is the long-range interaction term and the second term accounts for the short-range interaction. In standard long-range corrected functionals the short-range term is treated using DFT, while the long-range term is evaluated using HF exchange.[53] The failure of these functionals to correct core excitations can be rationalized. Long-range corrected functionals introduce HF exchange for terms in which r_{12} is large. For these terms either $\mathbf{r}_1$ or $\mathbf{r}_2$ must be large. Any of these exchange integrals that involve a core orbital will be vanishing small due to the fact that the core orbital is very short-ranged. Consequently, it is perhaps not surprising that such long-range corrected functionals have a negligible influence on core-excitation energies.

The logical conclusion from this analysis is that it is necessary to introduce HF exchange at short-range, *i.e.* when

r_{12} is small. The LCgau-DFT scheme partitions the $1/r_{12}$ operator as[59]

$$\frac{1}{r_{12}} = \frac{\mathrm{erfc}(\mu r_{12})}{r_{12}} - k\frac{2\mu}{\sqrt{\pi}}\exp^{-(1/a)\mu^2 r_{12}^2} + \frac{\mathrm{erf}(\mu r_{12})}{r_{12}} + k\frac{2\mu}{\sqrt{\pi}}\exp^{-(1/a)\mu^2 r_{12}^2} \quad (14)$$

where the first two terms describe the short-range interaction and the remaining terms give the long-range interaction. The inclusion of the Gaussian correction provides an additional contribution to the short-range term that can be tailored to introduce HF exchange at short-range.[42] This functional form was optimized, through the three parameters μ, k, and a, and tested on a set of core-excitation energies from first row nuclei, and the resulting functional was called LCgau-core-BOP.[42] Fig. 2 shows the variation in the proportion of HF exchange with r_{12}, and illustrates the increased proportion of HF exchange at short-range. However, it is likely to be advantageous to have a larger fraction of HF exchange at $r_{12} = 0$. To achieve this, in collaboration with Peach and Tozer, a short-range corrected functional that is based on a reversal of the standard long-range partitioning scheme was introduced.[48] In this functional, the electron repulsion operator is partitioned according to

$$\frac{1}{r_{12}} = C_{\mathrm{SHF}}\frac{\mathrm{erfc}(\mu_{\mathrm{SR}} r_{12})}{r_{12}} - C_{\mathrm{SHF}}\frac{\mathrm{erfc}(\mu_{\mathrm{SR}} r_{12})}{r_{12}} + C_{\mathrm{LHF}}\frac{\mathrm{erf}(\mu_{\mathrm{LR}} r_{12})}{r_{12}} - C_{\mathrm{LHF}}\frac{\mathrm{erf}(\mu_{\mathrm{LR}} r_{12})}{r_{12}} + \frac{1}{r_{12}} \quad (15)$$

Treating the first and third terms of eqn (15) with HF exchange and the remaining terms with DFT exchange leads to the following functional

$$E_{\mathrm{xc}}^{\mathrm{SRC1}} = C_{\mathrm{SHF}}E_{\mathrm{x}}^{\mathrm{SR-HF}}(\mu_{\mathrm{SR}}) - C_{\mathrm{SHF}}E_{\mathrm{x}}^{\mathrm{SR-DFT}}(\mu_{\mathrm{SR}}) + C_{\mathrm{LHF}}E_{\mathrm{x}}^{\mathrm{LR-HF}}(\mu_{\mathrm{LR}}) - C_{\mathrm{LHF}}E_{\mathrm{x}}^{\mathrm{LR-DFT}}(\mu_{\mathrm{LR}}) + E_{\mathrm{x}}^{\mathrm{DFT}} + E_{\mathrm{c}}^{\mathrm{DFT}} \quad (16)$$

where

$$E_{\mathrm{x}}^{\mathrm{LR-HF}} = -\frac{1}{2}\sum_{\sigma}\sum_{i,j}^{\mathrm{occ}}\iint \psi_{i\sigma}^{*}(\mathbf{r}_1)\psi_{j\sigma}^{*}(\mathbf{r}_1)\frac{\mathrm{erf}(\mu_{\mathrm{LR}} r_{12})}{r_{12}} \times \psi_{i\sigma}(\mathbf{r}_2)\psi_{j\sigma}(\mathbf{r}_2)\mathrm{d}\mathbf{r}_1\mathrm{d}\mathbf{r}_2 \quad (17)$$

and

$$E_{\mathrm{x}}^{\mathrm{SR-HF}} = -\frac{1}{2}\sum_{\sigma}\sum_{i,j}^{\mathrm{occ}}\iint \psi_{i\sigma}^{*}(\mathbf{r}_1)\psi_{j\sigma}^{*}(\mathbf{r}_1)\frac{\mathrm{erfc}(\mu_{\mathrm{SR}} r_{12})}{r_{12}} \times \psi_{i\sigma}(\mathbf{r}_2)\psi_{j\sigma}(\mathbf{r}_2)\mathrm{d}\mathbf{r}_1\mathrm{d}\mathbf{r}_2 \quad (18)$$

respectively. The long and short-range DFT exchange is computed from modifying the usual exchange energy[60]

$$E_{\mathrm{x}} = -\frac{1}{2}\sum_{\sigma}\int \rho_{\sigma}^{4/3}K_{\sigma}\mathrm{d}\mathbf{r} \quad (19)$$

to give

$$E_{\mathrm{x}}^{\mathrm{LR-DFT}} = -\frac{1}{2}\sum_{\sigma}\int \rho_{\sigma}^{4/3}K_{\sigma}\frac{8}{3}a_{\sigma} \times \left[\sqrt{\pi}\mathrm{erf}\left(\frac{1}{2a_{\sigma}^{\mathrm{LR}}}\right) + 2a_{\sigma}(b_{\sigma} - c_{\sigma})\right]\mathrm{d}\mathbf{r} \quad (20)$$

and

$$E_{\mathrm{x}}^{\mathrm{SR-DFT}} = -\frac{1}{2}\sum_{\sigma}\int \rho_{\sigma}^{4/3}K_{\sigma} \times \left\{1 - \frac{8}{3}a_{\sigma}\left[\sqrt{\pi}\mathrm{erf}\left(\frac{1}{2a_{\sigma}^{\mathrm{SR}}}\right) + 2a_{\sigma}(b_{\sigma} - c_{\sigma})\right]\right\}\mathrm{d}\mathbf{r} \quad (21)$$

where

$$a_{\sigma}^{\mathrm{SR}} = \frac{\mu_{\mathrm{SR}}}{6\sqrt{\pi}}\rho_{\sigma}^{-1/3}K_{\sigma}^{1/2} \quad (22)$$

$$a_{\sigma}^{\mathrm{LR}} = \frac{\mu_{\mathrm{LR}}}{6\sqrt{\pi}}\rho_{\sigma}^{-1/3}K_{\sigma}^{1/2} \quad (23)$$

$$b_{\sigma} = \exp\left(-\frac{1}{4a_{\sigma}^{2}}\right) - 1 \quad (24)$$

and

$$c_{\sigma} = 2a_{\sigma}^{2}b_{\sigma} + \tfrac{1}{2} \quad (25)$$

If $C_{\mathrm{LHF}} = 0$, the fraction of HF exchange will be C_{SHF} at $r_{12} = 0$, and fall to zero as r_{12} increases. This functional has two parameters, C_{SHF} and the attenuation parameter μ_{SR}, to be optimized. If $C_{\mathrm{LHF}} \neq 0$ the fraction of HF exchange approaches C_{LHF} at long-range. This form of the functional has four parameters, C_{SHF}, C_{LHF}, μ_{SR} and μ_{LR}, to be optimized. A closely related short-range corrected functional form was also considered

$$E_{\mathrm{xc}}^{\mathrm{SRC2}} = C_{\mathrm{SHF}}E_{\mathrm{x}}^{\mathrm{SR-HF}}(\mu_{\mathrm{SR}}) + (1 - C_{\mathrm{SHF}})E_{\mathrm{x}}^{\mathrm{SR-DFT}}(\mu_{\mathrm{SR}}) + C_{\mathrm{LHF}}E_{\mathrm{x}}^{\mathrm{LR-HF}}(\mu_{\mathrm{LR}}) + (1 - C_{\mathrm{LHF}})E_{\mathrm{x}}^{\mathrm{LR-DFT}}(\mu_{\mathrm{LR}}) + E_{\mathrm{c}}^{\mathrm{DFT}} \quad (26)$$

When $\mu_{\mathrm{SR}} = \mu_{\mathrm{LR}}$, this functional is equivalent to the SRC1 functional (eqn (16)). However, if $\mu_{\mathrm{SR}} \neq \mu_{\mathrm{LR}}$, the two functionals differ, and the SRC2 functional no longer corresponds to a rigorous partitioning of the electron–repulsion operator (eqn (15)).

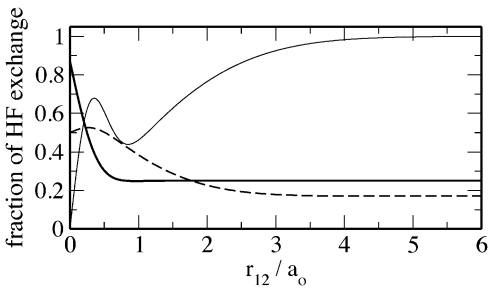

Fig. 2 Variation of the fraction of Hartree–Fock exchange. Narrow line: LCgau-core-BOP functional, broken line: SRC1 functional for first row nuclei, bold line: SRC1 functional for second row nuclei.

Table 2 Computed excitation energies (in eV) for core → valence transitions with a range of exchange–correlation functionals. Experimental data from ref. 107–116

Excitation	Exp.	B3LYP[b]	LCgau-core-BOP[c]	BH$^{0.58}$LYP[b]	CVR-B3LYP[d]	SRC1[b]	SRC2[b]
C_2H_4 C(1s) → π*	284.7	274.2	286.1	284.7	286.1	285.1	285.3
C_2H_2 C(1s) → π*	285.8	275.2	285.0	285.8	285.1	286.1	286.3
H_2CO C(1s) → π*	286.0	275.1	285.6	284.9	286.0	285.5	286.0
CO C(1s) → π*	287.4	276.1	286.5	285.5	286.9	286.1	286.7
N_2 N(1s) → π*	401.0	388.4	401.6	400.3	401.3	400.6	400.7
H_2CO O(1s) → π*	530.8	516.5	531.8	531.1	531.4	530.8	530.8
CO O(1s) → π*	534.2	519.6	535.2	534.7	534.5	534.4	534.2
HF F(1s) → σ*	687.4	669.3	686.4	687.4	686.0	686.7	686.9
MAD[a]	—	12.9	0.7	0.6	0.5	0.5	0.3

[a] Mean absolute deviation, [b] Ref. 48, [c] Ref. 42 and [d] Ref. 38.

These functionals were implemented in the Q-CHEM software package[61] and the parameters optimized using core excitations from first and second row nuclei. Excellent agreement with experiment was observed for excitations to valence and Rydberg orbitals. The source of this improvement lies with correcting the orbital energies for the core orbitals.[48] The short-range corrected functionals result in a lowering in the energy of the core orbitals while not affecting the energies of the valence orbitals, which in turn leads to an increase in the excitation energy through the first term in eqn (6). However, a disappointing feature of these functional forms was the same set of parameters could not be used for first and second row nuclei. The proportion of HF exchange in the functionals is also shown in Fig. 2. To obtain correct excitation energies for the second row nuclei requires a much greater fraction of HF exchange at $r_{12} = 0$ that falls rapidly, while a smaller fraction of HF exchange is required for the first row nuclei. Another feature of these functionals is that the functional no longer has the correct asymptotic behaviour at $r_{12} = \infty$. The form of the functional does not have sufficient flexibility to have a large fraction of HF exchange as $r_{12} \to 0$, fall rapidly and then rise again to 1 as r_{12} increases. For core-excitations, the errors introduced by the incorrect behaviour in the long-range are much smaller than the errors arising from the short-range and, consequently, fixing the short-range takes priority.

Tables 2 and 3 show reported core excitation energies[42,48] for core excitation energies to valence and Rydberg orbitals using a range of exchange–correlation functionals. Core excitation energies computed with B3LYP are much too low, indicating that 20% HF exchange is not sufficient. Overall, B3LYP has a mean absolute deviation (MAD) with experiment of 12.9 eV and 13.7 eV for the valence and Rydberg states, respectively. Also shown are results from B3LYP-like hybrid functional in which the fraction of HF exchange has been optimized. This yields a value of 58% HF exchange, with a correspondingly reduced proportion of B88 exchange of 39% and 8% Slater exchange. This functional is denoted BH$^{0.58}$LYP. This functional reduces the error in the excitation energies to 0.6 eV and 1.0 eV for excitations to valence and Rydberg orbitals, respectively. These results better represent the level accuracy that a hybrid functional with a fixed fraction of HF exchange can achieve, and provide benchmark values that can be used to assess any range-corrected functional. It is surprising that for predicting core excitation energies, this functional performs so well even when considering core excitations from different nuclei. The LCgau-core-BOP functional shows a similar level of error to BH$^{0.58}$LYP. The CVR-B3LYP and short-range corrected functionals reduce the MAD compared to BH$^{0.58}$LYP. The most accurate results are obtained with the SRC2 functional, with MADs of 0.3 eV and

Table 3 Computed excitation energies (in eV) for core → Rydberg transitions with a range of exchange–correlation functionals. Experimental data from ref. 107–116

Excitation	Exp.	B3LYP[b]	LCgau-core-BOP[c]	BH$^{0.58}$LYP[b]	CVR-B3LYP[d]	SRC1[b]	SRC2[b]
C_2H_4 C(1s) → 3s	287.1	275.7	288.1	288.3	288.0	287.8	287.9
C_2H_2 C(1s) → 3s	287.7	276.1	288.4	288.7	288.0	288.3	288.3
C_2H_2 C(1s) → $3p_\pi$	288.7	276.9	289.6	290.1	288.7	289.3	288.6
C_2H_2 C(1s) → $3p_\sigma$	288.8	276.5	288.4	289.5	288.2	288.8	289.2
H_2CO C(1s) → $3sa_1$	290.2	278.3	290.4	290.7	290.4	290.3	290.7
H_2CO C(1s) → $3pb_2$	291.3	279.4	291.4	291.5	290.8	291.1	291.4
CO C(1s) → 3s	292.4	279.4	291.7	292.4	291.0	291.7	292.0
CO C(1s) → $3p_\pi$	293.3	280.1	292.6	293.3	292.0	292.4	292.6
CO C(1s) → $3p_\sigma$	293.5	280.0	292.6	293.4	291.5	292.4	292.6
N_2 N(1s) → 3s	406.2	391.8	406.7	407.1	405.8	406.4	406.4
N_2 N(1s) → $3p_\pi$	407.1	392.5	407.7	408.2	406.1	407.2	407.1
N_2 N(1s) → $3p_\sigma$	407.3	392.5	408.0	408.4	405.7	407.2	407.2
H_2CO O(1s) → $3sa_1$	535.4	519.9	537.5	537.9	535.9	535.7	536.1
H_2CO O(1s) → $3pa_1$	536.3	520.7	538.5	538.5	536.4	537.3	536.9
CO O(1s) → 3s	538.9	522.6	539.7	540.1	538.1	539.2	539.0
CO O(1s) → $3p_\pi$	539.9	523.3	541.0	541.3	539.4	540.0	539.7
MAD[a]	—	13.7	0.9	1.0	0.7	0.5	0.5

[a] Mean absolute deviation, [b] Ref. 48, [c] Ref. 42 and [d] Ref. 38.

Table 4 Computed excitation energies in eV with oscillator strengths in parenthesis for the full and diagonal TDDFT **A** matrix

Excitation	Full **A**	Diagonal **A**
CO C(1s) → π*	286.1 (0.096)	287.4 (0.046)
CO C(1s) →3s	291.7 (0.004)	291.9 (0.001)
H_2CO O(1s) → π*	530.8 (0.060)	531.9 (0.033)
H_2CO O(1s) →3s	536.7 (0.002)	536.8 (0.000)
HCl Cl(1s) → σ*	2824.6 (0.004)	2825.4 (0.001)
HCl Cl(1s) →4p_π	2827.5 (0.001)	2827.6 (0.000)

0.5 eV. These functionals represent a significant improvement in the accuracy of the computed core excitation energies, and are approaching the level of accuracy achieved for traditional valence excitations.

For core excitations, the TDDFT matrix **A** (eqn (6)) is dominated by the diagonal elements. One option that would reduce significantly the cost of computing core excitation energies is to evaluate just the diagonal elements of **A**. Table 4 shows computed excitation energies and oscillator strengths for a small set of core-excited states computed with the full TDDFT matrix and with just the diagonal elements. The results show that for excitations to Rydberg states, this approximation introduces a small error. While this error is more significant for excitations to valence orbitals, such an approximation does hold promise for the study of the NEXAFS of large systems.

An alternative strategy to correcting for the approximate exchange in the exchange–correlation functional is to adopt methods that are based on exact exchange. CIS(D) provides a natural alternative to TDDFT that avoids the problem of approximate exchange, and we have investigated the application of the CIS(D) method to core excitations.[62] The CIS(D) method incorporates a perturbative doubles correction to the CIS excitation energies, and yields a significant improvement in the agreement with experiment. The CIS(D) correction to the excitation energy for a state with CIS excitation energy ω is[63,64]

$$\omega^{\mathrm{CIS(D)}} = -\frac{1}{4}\sum_{ijab}\frac{(u_{ij}^{ab})^2}{\Delta_{ij}^{ab}-\omega} + \sum_{ia} b_i^a v_i^a \qquad (27)$$

where

$$\Delta_{ij}^{ab} = \varepsilon_a + \varepsilon_b - \varepsilon_i - \varepsilon_j \qquad (28)$$

$$u_{ij}^{ab} = \sum_c [(ab \parallel cj)b_i^c - (ab \parallel ci)b_j^c] + \sum_k [(ka \parallel ij)b_k^b - (kb \parallel ij)b_k^a] \qquad (29)$$

$$v_i^a = \frac{1}{2}\sum_{jkbc}(jk \parallel bc)(b_i^a a_{jk}^{ca} + b_j^a a_{ik}^{cb} + 2b_j^b a_{ik}^{ac}) \qquad (30)$$

and a_{ij}^{ab} are the MP2 amplitudes

$$a_{ij}^{ab} = -\frac{(ij \parallel ab)}{\Delta_{ij}^{ab}} \qquad (31)$$

The first term in eqn (27) is termed the 'direct' contribution and accounts for electron correlation effects of the electron involved in the excitation, while the second 'indirect' term accounts for electron correlation effects between pairs of electrons not involved in the excitation.[65] CIS(D) has been extended to spin component scaled and scaled opposite spin versions, denoted SCS-CIS(D) and SOS-CIS(D), respectively.[65] These methods follow a similar approach to the SCS-MP2 method for ground states,[66,67] where the opposite and same spin components of the energy are scaled separately. Within SCS-CIS(D) the excitation energy can be considered as

$$\omega^{\mathrm{SCS-CIS(D)}} = c_U^{OS} w_U^{OS} + c_T^{OS} w_T^{OS} + c_U^{SS} w_U^{SS} + c_T^{SS} w_T^{SS} \qquad (32)$$

where OS and SS denote opposite and same spin, and w_U and w_T are the direct and indirect terms of eqn (27), respectively. For SOS-CIS(D), only the opposite spin components of eqn (32) are considered. Following optimization of the parameters an improved performance compared to CIS(D) was obtained.[65]

Application of standard CIS(D) (eqn (27)) to set of core excitations led to disappointing results for the calculation core excitation energies.[62] While the systematic underestimation of the core excitation energies was corrected, the predicted spectra were often qualitatively incorrect because of an underestimation of core excitations to Rydberg states relative to excitations to valence states. This is summed up by the observation that TDDFT predicts "correct spectra in the wrong place", CIS(D) gives "incorrect spectra in the right place". We have found that adopting a simplified opposite-spin approach including the direct term only gave a significant improvement in the calculated core excitation energies.[62] This is denoted cSOS-CIS(D), and can be expressed as

$$\omega^{\mathrm{cSOS-CIS(D)}} = c_U^{OS} w_U^{OS} \qquad (33)$$

with the parameter c_U^{OS} determined to be 1.42 from optimization a set of core excitation energies to reproduce experimental data. When used in conjunction with a large basis set, this gave a MAD from experiment for a set a core excitation energies from first and second row nuclei of 1.2 eV, which is greater than the errors achieved with short-range corrected functionals. The weakness of this approach is the need to correct the CIS(D) method through eqn (33) and the introduction of a parameter. CIS(D) is a second-order perturbative approximation to CCSD and it is this truncation that leads to the unbalanced treatment of core → valence and core → Rydberg excitations and the subsequent poor performance of CIS(D). These errors would be naturally corrected by the EOM-CCSD approach.[16]

An additional complication with the computation of core-excited states is that relativistic effects cannot be ignored. Relativistic effects lead to a significant lowering of the energy of core orbitals, while the energies of the valence orbitals remain roughly constant resulting in an increase in the excitation energy. This problem becomes particularly important when studying core excitations from heavier nuclei. We estimate such scaler relativistic effects by the change (lowering) of the orbital energy between relativistic and non-relativistic HF/cc-pCVTZ calculations where the relativistic energy was computed with the Douglas–Kroll–Hess Hamiltonian[68] implemented in MOLPRO.[69] In the applications presented here, all excitations from second row and transition metal

nuclei have been corrected for relativity in this way. A more desirable solution is to incorporate the relativistic corrections directly within the quantum chemical excited state calculation. The zero-order relativistic approximation (ZORA)[70,71] provides a simple approach through which this can be achieved. However, while scalar relativistic corrections may be sufficient for *K*-edge spectra, *L*-edge spectra are more complicated.[72] For *L*-edge spectra, core–hole spin–orbit interaction can be significant resulting in significant splitting of the spectral bands.[72,73] Furthermore, satellite transitions involving two or more electron excitations can occur. Within a DFT framework, these excitations can be described using a ΔKohn–Sham approach but are not described by single electron excitation methods, such as TDDFT and CIS, and are not considered in this work.

III. Benzene adsorbed on metal surfaces

The most important test for theoretical NEXAFS calculations is their application to current experimental problems. Today, most experimental NEXAFS work is concerned with complex systems rather than small molecules in the gas phase. NEXAFS is a particularly attractive technique in surface science because studies with linear polarized light can inform directly on the orientation and structure of an adsorbed molecule. Benzene adsorbed on metal surfaces is a prototypical system in surface science, and NEXAFS spectra have been reported for benzene adsorbed on several metal surfaces.[74–78] These systems provide an example of how NEXAFS spectroscopy can probe the nature of the bonding to the surface and the structure of the adsorbate. Benzene is physisorbed on the Au(111) surface and chemisorbed on the Pt(111) surface and the resulting NEXAFS spectra, which are shown in Fig. 3, differ significantly. On the Au(111) surface, the NEXAFS spectroscopy is dominated by a π* resonance that lies at 285.1 eV and is intense at grazing photon incidence and absent at normal photon incidence (see Fig. 4), a further weaker feature at 289.3 eV is also evident. On the Pt(111) surface a broader, less intense spectral band is observed. When chemisorbed on the surface, the hybridisation of the carbons atoms will change from sp^2 to sp^3 and so the resonance cannot be prescribed to excitation to a π* orbital. The variation in intensity of this feature with the photon angle of incidence indicated a bending of the C–H bonds out of the plane of the

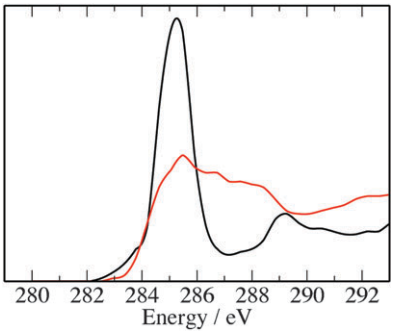

Fig. 3 Experimental NEXAFS spectra adapted from ref. 77 for benzene adsorbed on Au(111) (black line) and Pt(111) (red line) at grazing photon incidence.

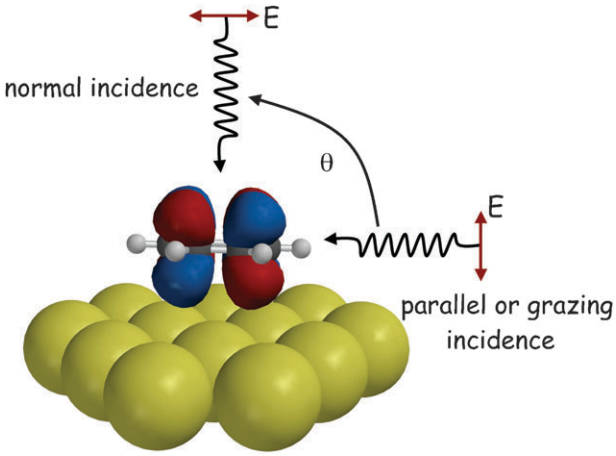

Fig. 4 Variation in the angle of incident radiation.

benzene ring. At normal photon incidence, a much weaker feature at about 287.5 eV is observed. Through calculations the nature of the observed resonances can be assigned and the variation of the spectra with the angle of the incidence radiation can be studied.

Before discussing the calculations for adsorbed benzene, it is informative to consider the NEXAFS of benzene in the gas phase. In experiment four prominent bands are observed below the ionization threshold.[79] These are referred to as A, B, C and D, and occur at 285.2 eV, 287.2 eV, 287.9 and 289.2 eV, respectively. Peak A is the most intense peak and is assigned to excitation to e_{2u} orbitals, which correspond to the lowest π* orbitals. However, there is less consensus in the literature over the assignment of the remaining peaks. Peak B has been assigned to Rydberg 3s[79] or σ* orbitals.[80,81] Similarly, peak C has been assigned to Rydberg 3p or 3d[79,82] or σ* orbitals.[80,81] Furthermore, peak D has been assigned to b_{2g}(π*) or Rydberg 3d, 4s or 4p excitations.[79–82] Fig. 5 shows computed spectra using TDDFT with B3LYP and SRC1 exchange–correlation functionals. For the B3LYP/6-311G* calculation, all excitation energies have been shifted by +10.7 eV to match experiment. The shifted spectrum is in good agreement with experiment, with an intense π* band with three weaker bands predicted at higher energies. However, the 6-311G* basis set does not contain diffuse basis functions, and is not designed for describing Rydberg states. Inclusion of a set of *s*, *p* and *d* Rydberg basis functions located at the center of the benzene ring, denoted 6-311G*+R, does not effect the intense π* band, but the energies and intensities of the weaker bands are changed significantly. For the B3LYP/6-311G*+R calculation, three weaker bands occur at 286.7, 287.2 and 289.1 eV (shifted by +10.7 eV). Overall, the agreement with the experimental spectrum is worse with the addition of the Rydberg basis functions, with the predicted Rydberg bands too low in energy. This is a consequence of the nature of the hybrid functional for which excitation energies to Rydberg states are expected to be too low.[83] The best agreement with experiment is obtained with the SRC1 functional for which it is not necessary to shift the computed spectrum. While the computed Rydberg bands are a little too high in energy, the overall shape of the experimental spectrum is reproduced well.

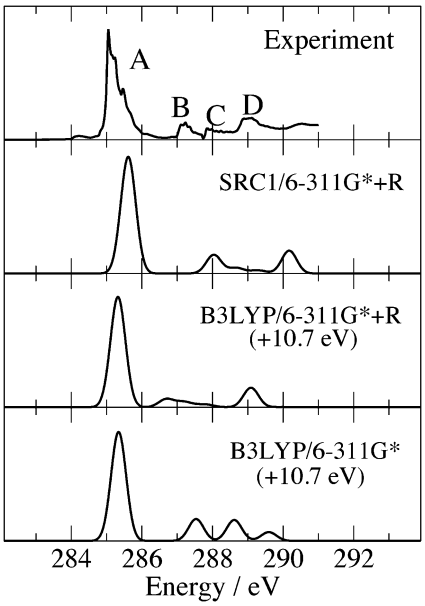

Fig. 5 Experimental and computed NEXAFS spectra of benzene in the gas phase. Experimental spectrum adapted from ref. 79.

Our calculations are consistent with the assignment of bands B, C and D to Rydberg excitations to 3s, 3p and 3d orbitals.[32]

We have applied TDDFT to study the NEXAFS spectroscopy of benzene on the Pt(111) and Au(111) surfaces.[32] These calculations consider benzene adsorbed on cluster models of the surface,[84] which are illustrated in Fig. 6. These calculations use the B3LYP functional with the 6-311G* + R basis set for benzene and the LANL2DZ basis set for the surface atoms, and the resulting spectra are shifted by +10.7 eV. Fig. 7 shows the computed spectra for benzene adsorbed on Au(111) and Pt(111) for a range of angles of photon incidence. For the Au(111) surface at grazing photon incidence (0°) an intense band arising from excitations to the $e_{2u}(\pi^*)$ orbitals of benzene is found at 285.4 eV (when shifted by +10.7 eV) with a weaker band arising from excitation to the $b_{2g}(\pi^*)$ orbitals of benzene at 290 eV. The relative positions and intensities of these bands are in good agreement with experiment. In comparison with the spectra of benzene in the gas phase there is no evidence of excitation to Rydberg states. For the Pt(111) surface at grazing photon incidence, the calculations predict a broad band centered at 285.8 eV (shifted by +10.7 eV), which in agreement with experiment is less intense than the band observed for Au(111). This band comprises excitations to a number of low lying virtual orbitals. The dominant contribution arises from excitation to orbitals that are localized on the benzene molecule and the surface that are described best as σ^*_{Pt-C} orbitals.[32] The orbitals lie along the Pt–C bonds and should be observed for grazing photon incidence. Overall, the agreement with experiment is not as good as for benzene on the Au(111) surface. This reflects the much more complex bonding to the surface that occurs on the Pt(111) surface and perhaps the lower quality of basis set used for the platinum atoms. However, the general features of the experimental spectrum are reproduced correctly.

As the angle of the incident radiation with the surface is increased, there is a reduction in the intensity of the observed bands. Even at relatively large angles the π* bands observed for the Au(111) surface remain evident. However, at normal incidence these bands are absent and only a weak feature at about 288 eV remains. In experiment, there is some evidence for a weak feature in this region at normal incidence. In terms of gas phase benzene, this band arises from excitation to an orbital, which is best described as the Rydberg 3s orbital, although it does have some σ^*_{C-H} character.

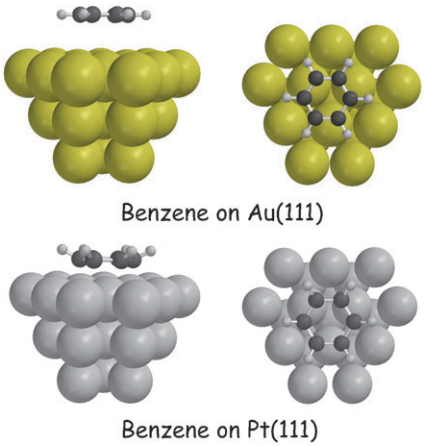

Fig. 6 Cluster models of benzene adsorbed on Au(111) and Pt(111) surfaces.

IV. Organic molecules adsorbed on semi-conductor surfaces

The adsorption of organic molecules on semiconductor surfaces has also been studied with NEXAFS. Unsaturated organic molecules bind strongly to these surfaces, and it has been proposed that these systems may form the basis of a new generation of electronic device within existing microelectronics technology.[85] Partly motivated by this potential, these systems have been the focus of many studies in recent years.

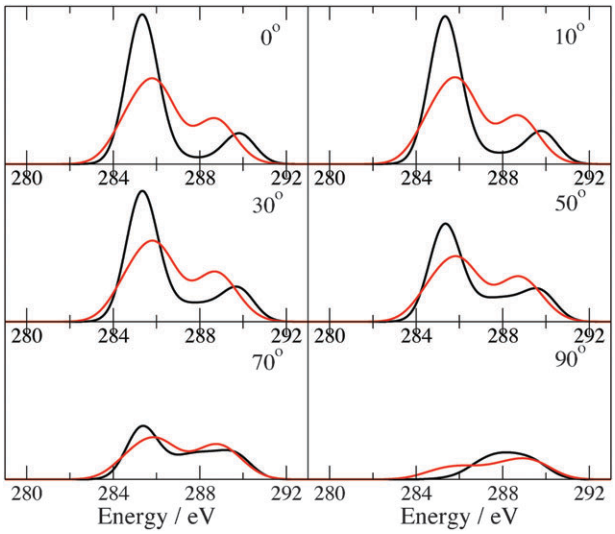

Fig. 7 Computed NEXAFS spectra of benzene adsorbed on Au(111) (black line) and Pt(111) (red line) for a range of angles of incident radiation.

The majority of this work has focused on the Si(100) surface. This surface undergoes a (2×1) reconstruction in which the exposed silicon atoms pair to form Si–Si dimers, which are reactive towards unsaturated organic molecules.

A fundamental problem is to establish the structure of the resulting adsorbed molecule. This is a problem that is well suited to NEXAFS, and NEXAFS has been used to study acetylene, ethylene and benzene on the Si(100)-2×1 surface.[86–91] A significant advance in this experimental work was the measurement of fully polarized spectra using a single domain Si(100) crystal which allowed the orientation of the adsorbed molecule with respect to the surface to be probed.[88,89,91] The carbon *K*-edge spectra for acetylene and benzene adsorbed on the surface are dominated by excitation to the π* orbitals. At higher energy, weaker features were observed that were assigned to excitations to the σ^*_{Si-C} and σ^*_{C-H} orbitals.

We reported TDDFT calculations of the NEXAFS spectra of acetylene, ethylene and benzene on the Si(100)-2×1 surface.[30] A modified hybrid exchange–correlation functional with 57% HF exchange was used in conjunction with a cluster model of the surface. This study showed that TDDFT can provide a reasonable description of the experimental spectra, reproducing the π*, σ^*_{Si-C} and σ^*_{C-H} resonances. In common with the molecules adsorbed on the metal surfaces, the transitions to Rydberg orbitals that are evident in the gas phase spectrum are no longer observed. More speculatively, calculations for benzene in different binding configurations showed changes in the location of the intense π* band of about 0.5 eV indicating that this band is sensitive to the binding configuration. More recently, this work was extended to study the adsorption of acetylene and benzene on the related group IV semiconductor surfaces C(100)-2×1 and Ge(100)-2×1.[92] The aim of this work was to study the sensitivity of the NEXAFS spectra of the adsorbed molecule to the underlying surface, and inform about the structure of the adsorbed molecules.

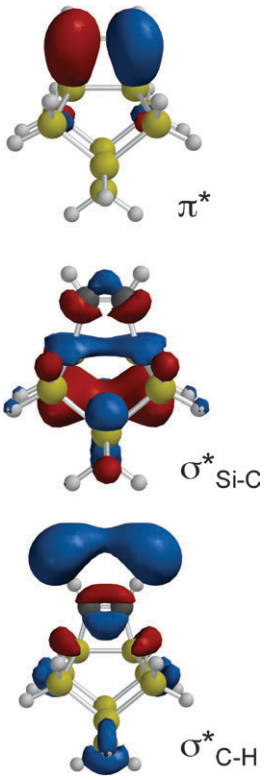

Fig. 8 Virtual orbitals of acetylene adsorbed on Si(100)-2×1.

Table 5 shows the computed excitation energies for excitation from the acetylene C(1s) orbitals to the π*, σ^*_{X-C} and σ^*_{C-H} orbitals, where X = C, Si or Ge, for acetylene adsorbed on cluster models of the surfaces. These orbitals are shown in Fig. 8. Excitation energies are shown for the B3LYP, $BH^{0.57}LYP$ and SRC1 exchange–correlation functionals, with the 6-311++G** basis set for the atoms comprising the adsorbed molecule and 6-311G** for the atoms of the surface. Also shown are values for the excitation energies for the Si(100)-2×1 surface from experiment. Both of the hybrid exchange–correlation functionals with modified exchange predict excitation energies that are close to experiment. There is a small improvement for the short-range corrected functional where the π* transition is predicted essentially correctly, and the remaining excitation energies are within 0.7 eV of experiment.

Having shown that the calculations can reproduce the reported experimental data, it can then be used to model and establish the properties of related systems which have yet to be studied. We have chosen to extend this work to the related surfaces C(100)-2×1 and Ge(100)-2×1.[92] The application of NEXAFS to study these surfaces is less common, however, studies of sulfur atoms adsorbed on Ge(100)-2×1 and hydrogenated C(100)-2×1 have been reported.[93,94] The calculations reveal subtle changes in the spectral features between the surfaces that can be understood in terms of the molecular orbitals of the adsorbed acetylene molecule. The C(1s) → π* excitation energy is dependent on the surface, and increases in the order Si(100)-2×1 < Ge(100)-2×1 < C(100)-2×1. This is shown by all three of the functionals used. This ordering can be rationalized by considering the C–C bond length of the adsorbed acetylene molecule. This bond length is shortest on the C(100)-2×1 surface and longest on the Si(100)-2×1 surface. Shortening of the C–C bond length will lead to a destablization of the π* orbital, and result in an increase in the associated core excitation energy. Excitation to the σ^*_{C-H} orbital shows little variation in excitation energy.

Table 5 Computed excitation energies and C–C bond lengths of acetylene adsorbed on the group IV semiconductor surfaces. Experimental results for the Si(100)-2×1 surface.[86,87]

Surface	π*/eV	σ^*_{C-H}/eV	σ^*_{X-C}/eV	r_{C-C}/Å
B3LYP				
C(100)-2×1	274.4	276.1	279.3	1.340
Si(100)-2×1	273.8	276.5	274.9	1.352
Ge(100)-2×1	274.1	276.4	274.9	1.344
$BH^{0.57}LYP$				
C(100)-2×1	284.3	288.0	289.5	1.340
Si(100)-2×1	283.8	288.2	286.7	1.352
Ge(100)-2×1	284.1	288.1	286.4	1.344
SRC1				
C(100)-2×1	285.3	288.2	289.4	1.340
Si(100)-2×1	284.8	288.1	286.7	1.352
Ge(100)-2×1	285.1	288.2	286.5	1.344
Experiment	284.7	287.6	286.0	

This orbital is localized on acetylene, and it is physically reasonable that it remains relatively unaffected by the precise nature of the surface. The σ^*_{X-C} orbital has a large contribution from the surface atoms, and the associated excitation is the most sensitive to the type of surface. The excitation energy is much higher for the C(100)-2×1 surface, and results in a change in the order of the σ^*_{C-H} and σ^*_{X-C} bands. This is likely to be a consequence of the greater strength of the adsorbate-surface C–C bonds compared to Si–C and Ge–C bonds.

V. Bioinorganic chemistry

While NEXAFS has been used extensively in surface science, it has also played a prominent role in other areas of research. The study of the structure and function of metalloproteins represents a major goal of bioinorganic chemistry. X-ray absorption spectroscopy can provide information on the oxidation state, coordination number and nature of the ground state wavefunction.[3,5] Spectra can be measured at the metal *K* and *L*-edge and the ligand *K*-edge. Much of this experimental work and subsequent analysis has been reported by Solomon and co-workers who have applied X-ray absorption spectroscopy to a wide range of systems.[3,95,96] Some of this work has been supplemented by quantum chemical calculations led by the group of Neese.

Our work in this area has focused on the X-ray absorption spectra of the oxidised form of blue copper proteins, such as plastocyanin.[26,97] These proteins are important in a number of important biological processes, such as photosynthesis.[98] The active site of plastocyanin is shown in Fig. 9 and comprises a copper centre coordinated with two histidine ligands, a cysteine ligand and a methionine ligand. The structure of the active site is characterised by a short Cu–S bond to cysteine and a long Cu–S bond to methionine. The oxidised form of the active site has a single occupied molecular orbital (SOMO) that is an out-of-phase combination of the Cu $3d_{x^2-y^2}$ and $S_{cys}3p_\pi$ orbitals. Excitation of core electrons to this singly occupied orbital appear as pre-edge features in the X-ray absorption spectrum.

Table 6 shows computed core excitation energies to the SOMO for the copper *K* and *L*-edges and the sulfur *K*-edge with TDDFT and ΔKohn–Sham approaches. The calculations use the geometry taken from the crystal structure (1PLC) and the 6-311(2+,2+)G** basis set. Unfortunately, this basis set is not available for copper, and the 6-31(2+,2+)G** basis set

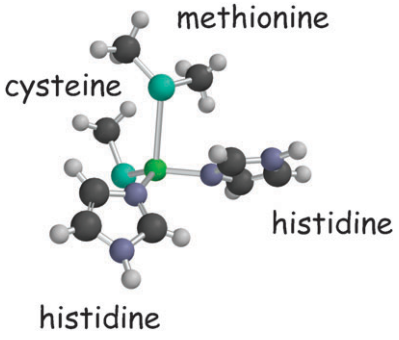

Fig. 9 Active site of plastocyanin.

Table 6 Computed core excitations energies in eV for plastocyanin

Excitation	Exp.[a]	TD-B3LYP	TD-SRC1	B3LYP	B3LYP[b]
Cu(1s) → SOMO	8978	8863	8978	8986	8980
Cu(2p) → SOMO	931	929	947	946	936
S(1s) → SOMO	2469	2417	2469	2465	2466

[a] Ref. 3, [b] Uncontracted basis functions.

was used for the copper atoms. The ΔKohn–Sham approach gives core excitation energies that are in reasonable agreement with experiment. However, the difference from experiment is many electron volts, particularly for the excitations from copper. In a recent study, it has been shown that using uncontracted basis functions leads to a significant improvement in core excitation energies computed within a ΔKohn–Sham approach.[26] For the *K*-edge excitations in plastocyanin, uncontracting the basis functions does result in an improvement in the calculated excitation energies and the results are in quite good agreement with experiment. The discrepancy for the Cu *L*-edge remains high. This is a result of the neglect of the 2p core–hole spin–orbit interaction which leads to two components.[73] The experimental value quoted is for the lower energy component of this excitation, and the calculations correctly predict a value that lies between the two components.

Now we consider the TDDFT calculations. Excitation energies for the B3LYP functional are, as expected, much lower than experiment. Due to its relatively high nuclear charge, this is particularly true for the Cu(1s) excitation, where an error of over 80 eV is observed. In contrast, the error for the excitation from the Cu 2p orbital is much lower. The 2p orbital of copper will be larger than the 1s orbital and can be thought of as less "core-like". Following the overlap arguments discussed in section II, there will be a greater overlap between the 2p orbital and the single occupied orbital, and consequently the failure of the B3LYP functional will be less dramatic. This presents a further problem to finding a universal exchange–correlation functional that can be applied to all core excitations since a functional designed for *K*-edge excitations is likely to fail for *L*-edge excitations. This is illustrated by calculations with the SRC1 short-range corrected functional. This functional predicts excitation energies for the Cu and S *K*-edges that are in excellent agreement with experiment. This is in some sense surprising for the Cu(1s) excitation, since this type of excitation was not present in the data that was used to parameterize the functional.[48] However, the excitation energy for the Cu-*L* edge is too high and is further from experiment than the calculation with the B3LYP functional.

For applications in bioinorganic chemistry accurate predictions of the excitation energy is desirable, but often the intensity of the transition is of more interest. From the intensity it is possible to extract information about the nature of the wavefunction of the SOMO. For blue copper proteins, the intensity of the pre-edge feature at the S *K*-edge can inform about the relative contribution of sulfur p orbital and copper d orbital character in the SOMO.[3] The SOMO in these proteins is a mixture of copper d and sulfur p orbitals. Since the s → p

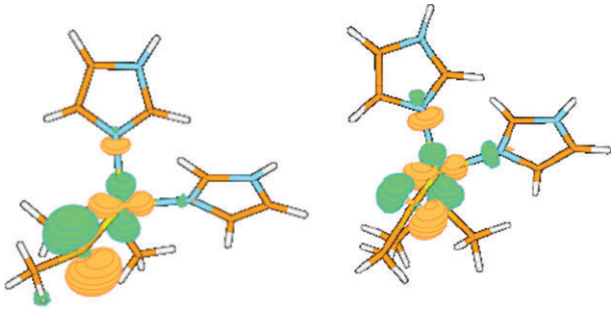

Fig. 10 Singly occupied molecular orbitals for plastocyanin (left) and cucumber basic protein (right).

transition is allowed and s → d is forbidden, the more intense the pre-edge feature, the greater the p character in the orbital. These intensities have been computed to be 0.0015 and 0.0011 for plastocyanin and the closely related blue copper protein cucumber basic protein, respectively.[97] This indicates that there is a greater p orbital character in the SOMO for plastocyanin. Fig. 10 shows molecular orbital pictures of the SOMOs of plastocyanin and cucumber basic protein plotted at the same contour surface. From these orbitals, the larger sulfur p component for plastocyanin can be identified clearly.

Another application of X-ray absorption spectroscopy is that it can identify different metal oxidation states. A systematic study of Cu(II)/Cu(III) oxidation states for a range of complexes showed that the feature arising from the Cu(1s)→ 3d transition is approximately 2 eV higher for Cu(III) compared to Cu(II).[99] One of the complexes included in this study was $[Cu^{III}(\mu\text{-}O)_2(L_{TEED})_2]^{2+}$/$[Cu^{II}(\mu\text{-}OH)_2(L_{TEED})_2]^{2+}$, for which excitation energies of 8980.84 eV and 8978.82 eV for the Cu(III) and Cu(II) complexes, respectively. Fig. 11 shows closely related complexes in which the ethyl groups from nitrogen have been replaced by methyl groups. TDDFT calculations with the SRC1 functional in conjunction with the 6-311G** basis set (6-31G* for copper) gives excitation energies of 8979.6 eV and 8978.6 eV for Cu(III) and Cu(II). The

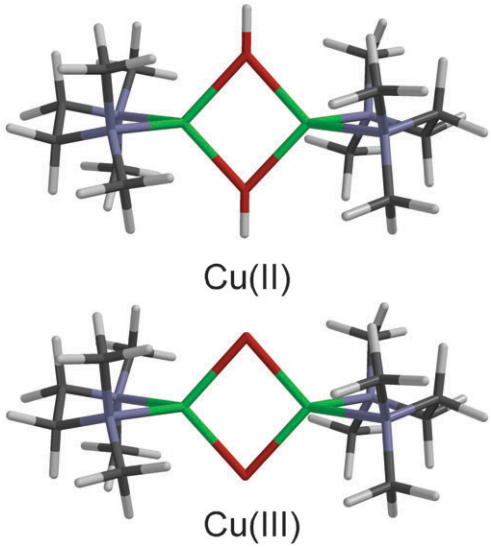

Fig. 11 Models of the $[Cu^{III}(\mu\text{-}O)_2(L_{TEED})_2]^{2+}$ and $[Cu^{II}(\mu\text{-}OH)_2\text{-}(L_{TEED})_2]^{2+}$ complexes.

calculations predict correctly a higher excitation energy for Cu(III) and reflect the lower energy of the Cu(1s) orbital in the Cu(III) complex.

VI. X-ray emission spectroscopy

X-ray emission spectra are simulated by computing the transition energy and the intensity, which is evaluated through the transition dipole moment.[100] The simplest approach to computing the intensity is to evaluate the transition dipole moment using the ground state orbitals, and this has been shown to give a surprisingly good agreement with experiment.[2,101] A physically more realistic approach is to use orbitals that account for the relaxation in the core-excited state. These can be obtained through ΔKohn–Sham or transition potential approaches. An illustration of this type of approach is a recent study of the XES of manganese coordination complexes.[102] As with the case of NEXAFS, for calculations of X-ray emission spectra that involve many transitions, it would also be convenient to use approaches such as TDDFT. To our knowledge, the application of TDDFT to XES has not been explored previously. In order to use TDDFT to study X-ray emission, we apply the TDDFT methodology directly to a Kohn–Sham determinant with a core hole generated using the MOM approach. This allows for the relaxation of the orbitals in the presence of the core hole, which has a significant effect on the computed emission energy. The X-ray emission transitions appear as negative eigenvalues. Since these excitations are the lowest energy roots of the TDDFT of EOM-CCSD equations, there is no need to limit the excitation subspace as required for NEXAFS calculations. A brief outline for the protocol for these calculations is summarized as follows:

1. Perform a calculation on the neutral ground state molecule.
2. Use the resulting molecular orbitals as the starting point for a further Kohn–Sham SCF calculation on the cation with a core hole in the relevant orbital, invoking MOM to prevent the collapse of the core hole during the SCF process.
3. Perform a TDDFT calculation.

To use the ground state orbitals in the X-ray emission calculations, the SCF optimization of the orbitals in step 2 can be bypassed. This protocol is not limited to TDDFT, and similar calculations can be performed using CIS and EOM-CCSD.

Table 7 shows X-ray emission energies computed using CIS, CIS(D), EOM-CCSD, ΔSCF with the B3LYP exchange–correlation functional and TDDFT with the BLYP, B3LYP and SRC1 functionals. For these calculations the 6-311G** basis set was used, and the calculations are performed using the ground state structure optimized at the MP2/cc-pVTZ level. The orbital labels describing the transition refer to the ground state of the molecule and not those of the cation with a core hole. The ΔKohn–Sham approach with the B3LYP functional has a MAD of 0.6 eV. which represents a satisfactory level of accuracy that is comparable to the accuracy achieved with ΔKohn–Sham calculations of core excitations.[26] Turning to the methods based on response theory, the MADs for CIS and TDDFT are much higher, with errors of many

Table 7 Computed X-ray emission energies (in eV). Experimental data from ref. 103, 117–121

Excitation	Exp.	CIS	CIS(D)	EOM-CCSD	ΔB3LYP	TD-BLYP	TD-B3LYP	TD-SRC1
CH_4 $1t_2 \rightarrow 1a_1$	276.3	269.8	275.6	276.2	276.8	286.4	283.3	279.5
C_2H_2 $1\pi_u \rightarrow 1\sigma_g$	278.9	272.6	280.5	279.7	280.4	289.5	286.2	282.1
C_2H_2 $3\sigma_g \rightarrow 1\sigma_g$	274.1	267.0	273.8	273.7	274.5	284.1	280.8	276.6
CO $5\sigma \rightarrow 2\sigma$	282.0	279.6	281.4	282.7	282.9	292.9	290.3	286.9
CO $1\pi \rightarrow 2\sigma$	278.4	271.9	281.7	278.6	280.0	288.9	285.3	279.9
CH_3OH $2a'' \rightarrow 2a'$	281.2	271.6	278.9	280.0	282.0	291.7	287.4	282.0
CH_3OH $7a' \rightarrow 2a'$	279.5	271.5	278.1	278.7	280.4	290.1	286.1	281.5
CH_3OH $6a' \rightarrow 2a'$	277.4	268.5	277.8	276.6	278.0	287.5	284.1	279.8
NH_3 $1e \rightarrow 1a_1$	388.8	380.3	387.1	388.0	388.2	399.5	395.8	390.8
NH_3 $2a_1 \rightarrow 1a_1$	395.1	389.7	394.6	395.6	395.3	406.3	403.0	399.0
H_2O $1b_1 \rightarrow 1a_1$	521.0	512.5	519.4	521.0	520.9	534.3	530.0	524.0
H_2O $3a_1 \rightarrow 1a_1$	525.1	518.2	524.2	525.4	525.0	538.2	534.3	528.9
H_2O $1b_2 \rightarrow 1a_1$	527.0	521.1	526.6	527.8	527.2	540.0	536.2	531.3
CH_3OH $2a'' \rightarrow 1a'$	527.8	521.0	527.4	528.0	528.2	541.3	536.7	531.5
CH_3OH $7a' \rightarrow 1a'$	526.1	518.3	525.4	526.0	526.6	540.3	535.1	529.2
CH_3OH $6a' \rightarrow 1a'$	523.9	513.0	522.3	522.7	524.1	537.9	532.4	525.0
CH_3F $5a_1 \rightarrow 1a_1$	675.6	667.1	675.4	674.9	675.5	691.7	686.1	679.2
CH_3F $2e \rightarrow 1a_1$	678.6	671.1	678.0	678.4	679.5	696.1	689.5	682.7
MAD[a]	—	7.3	1.1	0.5	0.6	12.2	8.1	3.0

[a] Mean absolute deviation.

electron volts. The emission energies computed with CIS are systematically underestimated, while those for TDDFT with BLYP and B3LYP functionals are systematically too large. The errors for TDDFT with the B3LYP functional are closer to experiment than with the BLYP functional, but remain too large. These results illustrate that X-ray emission energies computed with TDDFT are also sensitive to the fraction of HF exchange in the functional and indicate that the large errors observed are associated with the self-interaction error. However, in contrast to NEXAFS calculations, increasing the fraction of HF exchange results in a decrease in the emission energies. Application of the SRC1 functional that was parameterized for X-ray absorption does lead to an improvement in the predicted emission energies. However, an overall MAD of 3.0 eV remains too high and could certainly be improved by direct parameterization on emission energies.

Also shown are results for correlated *ab initio* methods CIS(D) and EOM-CCSD. The CIS(D) emission energies are improved significantly with respect to CIS. The MAD of 7.3 eV for CIS reduced to 1.1 eV. The most accurate emission energies are predicted by EOM-CCSD with a MAD of 0.5 eV. However, for this approach we have found that it can be problematic to converge the CCSD calculation for the wavefunction with a core hole. This has been discussed in detail elsewhere, and practical solutions have been described.[16] Despite this current limitation, EOM-CCSD does provide accurate X-ray emission energies where it can be applied.

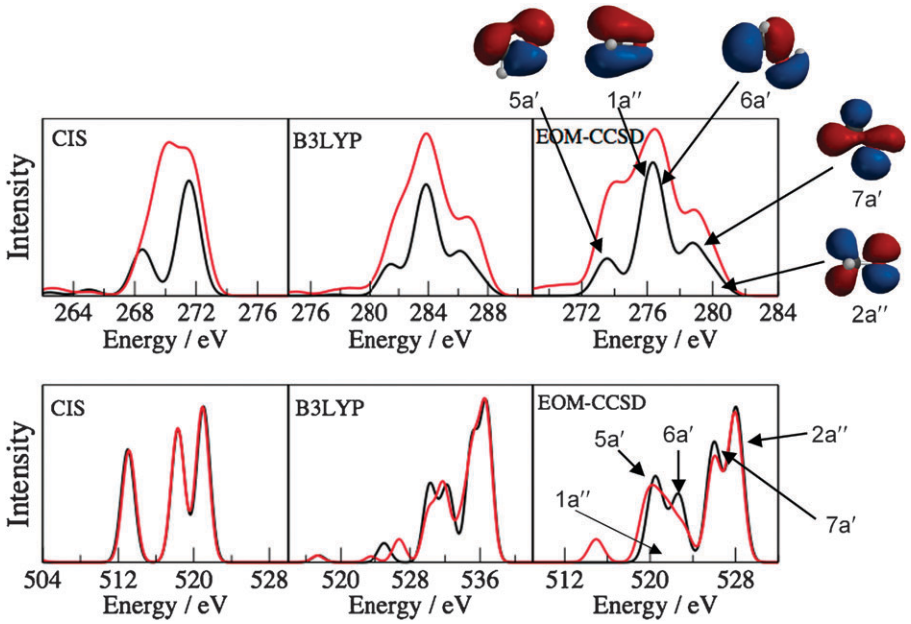

Fig. 12 Computed C-*K* (top panels) and O-*K* (lower panels) X-ray emission spectra for methanol (black line) and ethanol (red line).

An important test for these methods is the calculation of experimental spectra, since it is also important to predict the intensity accurately. Fig. 12 shows X-ray emission spectra computed using CIS, TDDFT with the B3LYP functional and EOM-CCSD with the 6-311G** basis set for methanol and ethanol. For the EOM-CCSD spectra, excitation energies computed with EOM-CCSD have been combined with intensities from the TDDFT calculations. Spectra were generated by representing the transitions with Gaussian functionals with a full-width at half maximum of 1 eV. For these molecules, high quality carbon-*K* and oxygen-*K* experimental spectra have been reported,[103] and these are depicted in Fig. 13. The assignment of the bands in these spectra has been discussed in detail in the earlier theoretical work of Larkins and co-workers who studied the X-ray emission in these molecules using transition energies and orbitals from HF calculations.[104,105] The X-ray emission of methanol has also been studied using optimized multiconfigurational wavefunctions.[106] Initially, we will discuss the results for the O-*K* spectrum. For methanol the experimental spectrum has four distinct peaks at 527.8 eV, 526.1 eV, 523.9 eV and 521.5 eV which are assigned to the 2a″, 7a′, 6a′ and 5a′ orbitals, respectively. The 1a″ band is weaker and lies at 522.4 eV. The EOM-CCSD based spectrum reproduces the experiment well, with computed excitation energies of 528.0 eV, 526.0 eV, 522.7 eV, 521.2 eV, 520.4 eV for the 2a″, 7a′, 6a′, 1a″ and 5a′ orbitals. B3LYP also gives a computed spectrum that reproduces the experimental spectral profile well, while the CIS spectrum does differ significantly from experiment. Similar to experiment, the predicted spectra for ethanol show only small deviations from methanol. In experiment the C-*K* spectrum shows four distinct peaks at 282.9 eV, 281.2 eV, 279.5 eV and 276.6 eV. The computed EOM-CCSD spectra has only three peaks and the agreement with experiment is not as good as for the O-*K* spectrum. The computed spectrum does agree well with the computed spectrum of Larkins and Seen,[104] and in this work it was suggested that the deviation from experiment is most likely due to satellite contributions and the presence of impurities.

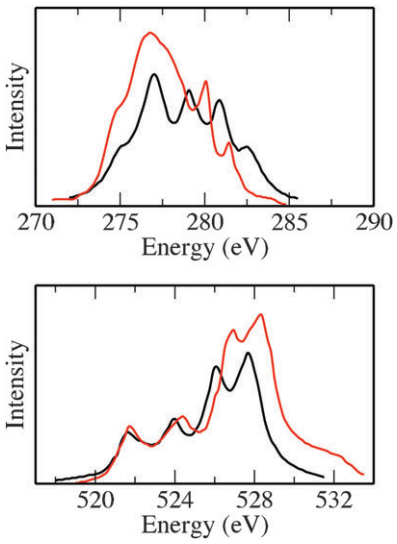

Fig. 13 Experimental C-*K* (top panel) and O-*K* (lower panel) X-ray emission spectra for methanol (black line) and ethanol (red line). Adapted from ref. 103.

VII. Conclusions and future directions

The application of spectroscopic techniques in the X-ray region is becoming increasingly common across a wide range of research areas. This work has benefited from the availability of new light sources with increased resolution and intensity. Accurate calculations of X-ray absorption and emission spectra provide an extremely useful tool that can be used alongside experimental measurements. Quantum chemical excited state methods such as TDDFT are used routinely to study electronic excitations in the UV region, and the application of such methods to the problem of core excitations has the prospect to provide accurate predictions of NEXAFS spectra at a relatively low computational cost that can be used by non-specialist users. The application of standard exchange–correlation functionals to the problem of core-excitations leads to a large discrepancy with experiment. The development of exchange–correlation functionals to treat core excitations have focused on the description of exchange in the functional, and have resulted in a much closer agreement with experiment.

Through several applications we have illustrated how these calculations can be applied to a range of problems. These calculations demonstrate that NEXAFS does provide a subtle probe of adsorbed molecules and elucidate the nature of the surface–adsorbate interaction, providing direct structural information. Some of these effects are illustrated by small changes in the NEXAFS spectra, and present a challenge to both experimental measurements and calculations. Furthermore, TDDFT calculations can accurately reproduce the pre-edge features observed in the spectra of complex biological molecules and dependence of the core-excitation energy on the oxidation state. However, a completely satisfactory solution to the problem of computing core-excitations with TDDFT has yet to be achieved. Currently, the most accurate functionals rely on parameters that are fitted to experimental data and a single solution that can be applied to all types of core excitations is elusive. The EOM-CCSD method would provide one possibility. However, this method has not been adapted to study core excitations directly. For core excitations from heavier nuclei the significance of relativistic effects becomes more prominent and the direct incorporation of these effects within the NEXAFS calculations is important.

Another important development of these methods is the application to X-ray emission spectroscopy. We have shown that this can be achieved by applying CIS, TDDFT or EOM-CCSD methods to a wavefunction or Kohn–Sham determinant with a core hole. A number of similarities between the calculations of X-ray absorption and emission energies emerge. Within TDDFT, standard exchange–correlation functionals predict emission energies that are significantly different from experiment and new developments in functionals are required. The EOM-CCSD method does provide accurate X-ray emission energies and when applied to the X-ray emission spectra of methanol and ethanol, good agreement with experiment and previous theoretical work is obtained.

This review has described the current state of the art in quantum chemical calculations of X-ray absorption and X-ray emission spectra, illustrating what can be achieved and highlighting current deficiencies and areas for further development. Many of these methods are available in modern quantum chemical packages and we hope this review will provide a catalyst for interested researchers to use them in their own research.

Acknowledgements

FAA would like to acknowledge the Papua Government for a PhD studentship grant. The authors are also grateful to the University of Nottingham for access to its high performance computing facility.

References

1 J. Stöhr, *NEXAFS Spectroscopy, Springer Series in Surface Science*, Springer, Heidelberg, 1996.
2 A. Nilsson and L. G. M. Pettersson, *Surf. Sci. Rep.*, 2004, **55**, 49.
3 E. I. Solomon, R. K. Szilagyi, S. D. George and L. Basumallick, *Chem. Rev.*, 2004, **104**, 419.
4 J. E. Penner-Hahn, *Coord. Chem. Rev.*, 2005, **249**, 161.
5 J. Yano and V. K. Yachandra, *Photosynth. Res.*, 2009, **102**, 241.
6 G. Hahner, *Chem. Soc. Rev.*, 2006, **35**, 1244.
7 P. Wernat, D. Nordlund, U. Bergmann, M. Cavalleri, H. Ogasawara, L. A. Naslund, T. K. Hirsch, L. Ojamae, P. Glatzel, L. G. M. Pettersson and A. Nilsson, *Science*, 2004, **304**, 995.
8 T. Tokushima, Y. Harada, O. Takahashi, Y. Senba, H. Ohashi, L. G. M. Pettersson, A. Nilsson and S. Shin, *Chem. Phys. Lett.*, 2008, **460**, 387.
9 W. J. Hunt and W. A. Goddard III, *Chem. Phys. Lett.*, 1969, **3**, 414.
10 H. Ågren, V. Carravetta, O. Vahtras and L. G. M. Pettersson, *Chem. Phys. Lett.*, 1994, **222**, 75.
11 H. Ågren, V. Carravetta, O. Vahtras and L. G. M. Pettersson, *Theor. Chem. Acta*, 1997, **97**, 14.
12 A. Stener, M. Lisini and P. Decleva, *Chem. Phys.*, 1995, **191**, 141.
13 L. Triguero, L. G. M. Pettersson and H. Ågren, *Phys. Rev. B: Condens. Matter Mater. Phys.*, 1998, **58**, 8097.
14 M. Nyberg, Y. Luo, L. Triguero and L. G. M. Pettersson, *Phys. Rev. B: Condens. Matter Mater. Phys.*, 1999, **60**, 7956.
15 J. J. Rehr and A. L. Ankudinov, *Coord. Chem. Rev.*, 2005, **249**, 131.
16 M. Nooijen and R. J. Bartlett, *J. Chem. Phys.*, 1995, **102**, 6735.
17 K. Ueda, M. Hoshino, T. Tanaka, M. Kitajima, H. Tanaka, A. De Fanis, Y. Tamenori, M. Ehara, F. Oyagi, K. Kuramoto and H. Nakatsuji, *Phys. Rev. Lett.*, 2005, **94**, 243004.
18 K. Kuramoto, M. Ehara, H. Nakatsuji, M. Kitajima, H. Tanaka, A. De Fanis, Y. Tamenori and K. Ueda, *J. Electron Spectrosc. Relat. Phenom.*, 2005, **142**, 253.
19 K. Kuramoto, M. Ehara and H. Nakatsuji, *J. Chem. Phys.*, 2005, **122**, 014304.
20 M. Ehara, H. Nakatsuji, M. Matsumoto, T. Hatamoto, X.-J. Liu, T. Lischke, G. Prumper, T. Tanaka, C. Makochekanwa, M. Hoshino, H. Tanaka, J. R. Harries, Y. Tamenori and K. Ueda, *J. Chem. Phys.*, 2006, **124**, 124311.
21 T. Tanaka, K. Ueda, R. Feifel, L. Karlsson, H. Tanaka, M. Hoshino, M. Kitajima, M. Ehara, R. Fukuda, R. Tamaki and H. Nakatsuji, *Chem. Phys. Lett.*, 2007, **435**, 182.
22 P. S. Bagus, *Phys. Rev.*, 1965, **139**, A619.
23 H. Hsu, E. R. Davidson and R. M. Pitzer, *J. Chem. Phys.*, 1976, **65**, 609.
24 A. Naves de Brito, N. Correla, S. Svensson and H. Ågren, *J. Chem. Phys.*, 1991, **95**, 2965.
25 A. T. B. Gilbert, N. A. Besley and P. M. W. Gill, *J. Phys. Chem. A*, 2008, **112**, 13164.
26 N. A. Besley, A. T. B. Gilbert and P. M. W. Gill, *J. Chem. Phys.*, 2009, **130**, 124308.
27 A. Dreuw and M. Head-Gordon, *Chem. Rev.*, 2005, **105**, 4009.
28 S. Hirata and M. Head-Gordon, *Chem. Phys. Lett.*, 1999, **314**, 291.
29 M. Stener, G. Fronzoni and M. de Simone, *Chem. Phys. Lett.*, 2003, **373**, 115.
30 N. A. Besley and A. Noble, *J. Phys. Chem. C*, 2007, **111**, 3333.
31 S. D. George, T. Petrenko and F. Neese, *Inorg. Chim. Acta*, 2008, **361**, 965.
32 F. A. Asmuruf and N. A. Besley, *J. Chem. Phys.*, 2008, **129**, 064705.
33 T. Tsuchimochi, M. Kobayashi, A. Nakata, Y. Imamura and H. Nakai, *J. Comput. Chem.*, 2008, **29**, 2311.
34 U. Ekström and P. Norman, *Phys. Rev. A: At., Mol., Opt. Phys.*, 2006, **74**, 042722.
35 U. Ekström, P. Norman, V. Carravetta and H. Ågren, *Phys. Rev. Lett.*, 2006, **97**, 143001.
36 Y. Imamura, T. Otsuka and H. Nakai, *J. Comput. Chem.*, 2007, **28**, 2067.
37 A. Nakata, Y. Imamura, T. Ostuka and H. Nakai, *J. Chem. Phys.*, 2006, **124**, 094105.
38 A. Nakata, Y. Imamura and H. Nakai, *J. Chem. Phys.*, 2006, **125**, 064109.
39 A. Nakata, Y. Imamura and H. Nakai, *J. Chem. Theory Comput.*, 2007, **3**, 1295.
40 G. Tu, Z. Rinkevicius, O. Vahtras, H. Ågren, U. Ekström, P. Norman, V. Carravetta, U. Elkström and P. Norman, *Phys. Rev. A: At., Mol., Opt. Phys.*, 2007, **76**, 022506.
41 Y. Imamura and H. Nakai, *Int. J. Quantum Chem.*, 2007, **107**, 23.
42 J.-W. Song, M. A. Watson, A. Nakata and K. Hirao, *J. Chem. Phys.*, 2008, **129**, 184113.
43 A. Dreuw, J. Weisman and M. Head-Gordon, *J. Chem. Phys.*, 2003, **119**, 2943.
44 M. J. G. Peach, P. Benfield, T. Helgaker and D. J. Tozer, *J. Chem. Phys.*, 2008, **128**, 044118.
45 G. Fronzoni, R. De Francesco and M. Stener, *J. Phys. Chem. B*, 2005, **109**, 10332.
46 G. Fronzoni, R. De Francesco and M. Stener, *J. Phys. Chem. B*, 2006, **110**, 9899.
47 Y. Imamura and H. Nakai, *Chem. Phys. Lett.*, 2006, **419**, 297.
48 N. A. Besley, M. J. G. Peach and D. J. Tozer, *Phys. Chem. Chem. Phys.*, 2009, **11**, 10350.
49 A. D. Becke, *Phys. Rev. A: At., Mol., Opt. Phys.*, 1988, **38**, 3098.
50 P. A. M. Dirac, *Proc. Cam. Phil. Soc.*, 1930, **26**, 376.
51 C. Lee, W. Yang and R. G. Parr, *Phys. Rev. B: Condens. Matter*, 1988, **37**, 785.
52 S. H. Vosko, L. Wilk and M. Nusair, *Can. J. Phys.*, 1980, **58**, 1200.
53 Y. Tawada, T. Tsuneda, S. Yanagisawa, T. Yanai and K. Hirao, *J. Chem. Phys.*, 2004, **120**, 8425.
54 T. Yanai, D. P. Tew and N. C. Handy, *Chem. Phys. Lett.*, 2004, **393**, 51.
55 M. J. G. Peach, A. J. Cohen and D. J. Tozer, *Phys. Chem. Chem. Phys.*, 2006, **8**, 4543.
56 J.-D. Chai and M. Head-Gordon, *J. Chem. Phys.*, 2008, **128**, 084106.
57 J.-D. Chai and M. Head-Gordon, *Chem. Phys. Lett.*, 2008, **467**, 176.
58 M. A. Rohrdanz, K. M. Martins and J. M. Herbert, *J. Chem. Phys.*, 2009, **130**, 054112.
59 J.-W. Song, S. Tokura, T. Sato, M. A. Watson and K. Hirao, *J. Chem. Phys.*, 2007, **127**, 154109.
60 J.-W. Song, T. Hirosawa, T. Tsuneda and K. Hirao, *J. Chem. Phys.*, 2007, **126**, 154105.
61 Y. Shao, L. F. Molnar, Y. Jung, J. Kussmann, C. Ochsenfeld, S. T. Brown, A. T. B. Gilbert, L. V. Slipchenko, S. V. Levchenko, D. P. O'Neill, R. A. Di Stasio Jr, R. C. Lochan, T. Wang, G. J. O. Beran, N. A. Besley, J. M. Herbert, C. Y. Lin, T. V. Voorhis, S.-H. Chien, A. Sodt, R. P. Steele, V. A. Rassolov, P. E. Maslen, P. P. Korambath, R. D. Adamson, B. Austin, J. Baker, E. F. C. Byrd, H. Dachsel, R. J. Doerksen, A. Dreuw, B. D. Dunietz, A. D. Dutoi, T. R. Furlani, S. R. Gwaltney, A. Heyden, S. Hirata, C.-P. Hsu, G. Kedziora, R. Z. Khalliulin, P. Klunzinger, A. M. Lee, M. S. Lee, W. Liang, I. Lotan, N. Nair, B. Peters, E. I. Proynov, P. A. Pieniazek, Y. M. Rhee,

J. Ritchie, E. Rosta, C. D. Sherrill, A. C. Simmonett, J. E. Subotnik, H. L. Woodcock III, W. Zhang, A. T. Bell, A. K. Chakraborty, D. M. Chipman, F. J. Keil, A. Warshel, W. J. Hehre, H. F. Schaefer III, J. Kong, A. I. Krylov, P. M. W. Gill and M. Head-Gordon, *Phys. Chem. Chem. Phys.*, 2006, **8**, 3172.
62 F. A. Asmuruf and N. A. Besley, *Chem. Phys. Lett.*, 2008, **463**, 267.
63 M. Head-Gordon, R. J. Rico, M. Oumi and T. J. Lee, *Chem. Phys. Lett.*, 1994, **219**, 21.
64 M. Head-Gordon, D. Maurice and M. Oumi, *Chem. Phys. Lett.*, 1995, **246**, 114.
65 Y. M. Rhee and M. Head-Gordon, *J. Phys. Chem. A*, 2007, **111**, 5314.
66 S. Grimme, *J. Chem. Phys.*, 2003, **118**, 9095.
67 S. Grimme and E. I. Izgorodina, *Chem. Phys.*, 2004, **305**, 223.
68 M. Reiher and A. Wolf, *J. Chem. Phys.*, 2004, **121**, 2037.
69 MOLPRO, version 2006.1, a package of *ab initio* programs, H.-J. P. Werner, P. J. Knowles, R. Lindh, F. R. Manby, M. Schütz, P. Celani, T. Korona, G. Rauhut, R. D. Amos, A. Bernhardsson, A. Berning, D. L. Cooper, M. J. O. Deegan, A. J. Dobbyn, F. Eckert, C. Hampel, G. Hetzer, A. W. Lloyd, S. J. McNicholas, W. Meyer, M. E. Mura, A. Nicklass, P. Palmieri, R. Pitzer, U. Schumann, H. Stoll, A. J. Stone, R. Tarroni and T. Thorsteinsson.
70 E. van Lenthe, E. J. Baerends and J. G. Snijders, *J. Chem. Phys.*, 1993, **99**, 4597.
71 E. van Lenthe, E. J. Baerends and J. G. Snijders, *J. Chem. Phys.*, 1994, **101**, 9783.
72 U. Ekström, P. Norman and V. Carravetta, *Phys. Rev. A: At., Mol., Opt. Phys.*, 2006, **73**, 022501.
73 S. J. George, M. D. Lowery, E. I. Solomon and S. P. Cramer, *J. Am. Chem. Soc.*, 1993, **115**, 2968.
74 J. A. Horsley, J. Stöhr, A. P. Hitchcock, D. A. Newbury, A. L. Johnson and F. Sette, *J. Chem. Phys.*, 1985, **83**, 6099.
75 A. C. Liu, J. Stöhr, C. M. Friend and R. J. Madix, *Surf. Sci.*, 1990, **235**, 107.
76 A. C. Liu, C. M. Friend and J. Stöhr, *Surf. Sci.*, 1990, **236**, L349.
77 K. Weiss, S. Gerbert, M. Wühn, H. Wadepohl and Ch. Wöll, *J. Vac. Sci. Technol., A*, 1998, **16**, 1017.
78 Ch. Wöll, *J. Synchrotron Radiat.*, 2001, **8**, 129.
79 E. E. Rennie, B. Kempgens, H. M. Köppe, U. Hergenhahn, J. Feldhaus, B. S. Itchkawitz, A. L. D. Kilcoyne, A. Kivimäki, K. Maier, M. N. Piancastelli, M. Polcik, A. Rüdel and A. M. Bradshaw, *J. Chem. Phys.*, 2000, **113**, 7362.
80 R. Püttner, C. Kolczewski, M. M. Martins, A. S. Schlacter, G. Snell, M. Sant'Anna, M. Viefhaus, K. Hermann and G. Kaindl, *Chem. Phys. Lett.*, 2004, **393**, 361.
81 C. Kolczewski, R. Püttner, M. Martins, A. S. Schlacter, G. Snell, M. Sant' Anna, K. Hermann and G. Kaindl, *J. Chem. Phys.*, 2006, **124**, 034302.
82 W. H. E. Schwarz, T. C. Chang, U. Seeger and K. H. Hwang, *Chem. Phys.*, 1987, **117**, 73.
83 D. J. Tozer and N. C. Handy, *Chem. Phys.*, 1998, **109**, 10180.
84 N. A. Besley, *Chem. Phys.*, 2005, **122**, 184706.
85 J. Chen, M. A. Reed, A. M. Rawlett and J. M. Tour, *Science*, 1999, **286**, 1550.
86 F. Matsui, H. W. Yeom, A. Imanishi, K. Isawa, I. Matsuda and T. Ohta, *Surf. Sci.*, 1998, **401**, L413.
87 F. Matsui, H. W. Yeom, I. Matsuda and T. Ohta, *Phys. Rev. B: Condens. Matter Mater. Phys.*, 2000, **62**, 5036.
88 F. Hennies, A. Föhlisch, W. Wurth, N. Witkowski, M. Nagasono and M. N. Piancastelli, *Surf. Sci.*, 2003, **529**, 144.
89 A. Pietzsch, F. Hennies, A. Föhlisch, W. Wurth, M. Nagasono, N. Witkowski and M. N. Piancastelli, *Surf. Sci.*, 2004, **562**, 65.
90 M. J. Kong, A. V. Teplyakov, J. G. Lyubovitsky and S. F. Bent, *Surf. Sci.*, 1998, **411**, 286.
91 N. Witkowski, F. Hennies, A. Pietzsch, S. Mattsson, A. Föhlisch, W. Wurth, M. Nagasono and M. N. Piancastelli, *Phys. Rev. B: Condens. Matter Mater. Phys.*, 2003, **68**, 115408.
92 F. A. Asmuruf and N. A. Besley, *Surf. Sci.*, 2009, **603**, 158.
93 K. Newstead, A. W. Robinson, S. d'Addato, A. Patchett, N. P. Prince, R. McGrath, R. Whittle, E. Dudzik and I. T. McGovern, *Surf. Sci.*, 1993, **287–288**, 317.
94 A. Hoffmann, G. Comtet, L. Hellner, G. Dujardin and M. Petravic, *Appl. Phys. Lett.*, 1998, **73**, 1152.
95 T. Glaser, B. Hedman, K. O. Hodgson and E. I. Solomon, *Acc. Chem. Res.*, 2000, **33**, 859.
96 K. Ray, DeBeer, S. George, K. I. Solomon, K. Wieghardt and F. Neese, *Acc. Chem. Res.*, 2007, **13**, 2783.
97 D. Robinson and N. A. Besley, *Phys. Chem. Chem. Phys.*, 2010, DOI: 10.1039/C001805H.
98 H. B. Gray and E. I. Solomon, *Copper Proteins*, ed. T. G. Spiro, Wiley, New York, 1981.
99 J. L. DuBois, P. M. Mukherjee, T. D. P. Stack, B. Hedman, E. I. Solomon and K. O. Hodgson, *J. Am. Chem. Soc.*, 2000, **122**, 5775.
100 T. Mukoyama, *Spectrochim. Acta, Part B*, 2004, **59**, 1107.
101 L. Triguero, L. G. M. Pettersson and H. Ågren, *J. Phys. Chem.*, 1998, **102**, 10599.
102 G. Smolentsev, A. V. Soldatov, J. Messinger, K. Merz, Weyhermüller, U. Bergmann, Y. Pushkar, J. Yani, V. K. Yachandra and P. Glatzel, *J. Am. Chem. Soc.*, 2009, **131**, 13161.
103 J. E. Rubensson, N. Wassdahl, R. Brammer and J. Nordgren, *J. Electron Spectrosc. Relat. Phenom.*, 1988, **47**, 131.
104 F. P. Larkins and A. J. Seen, *Phys. Scr.*, 1990, **41**, 827.
105 A. J. Seen and F. P. Larkins, *J. Phys. B: At., Mol. Opt. Phys.*, 1992, **25**, 4811.
106 H. Ågren and A. Flores-Riveros, *J. Electron Spectrosc. Relat. Phenom.*, 1991, **56**, 259.
107 M. Tronc, G. C. King and F. H. Read, *J. Phys. B: At. Mol. Phys.*, 1979, **12**, 137.
108 M. Tronc, G. C. King and F. H. Read, *J. Phys. B: At. Mol. Phys.*, 1980, **13**, 999.
109 A. P. Hitchcock and C. E. Brion, *J. Phys. B: At. Mol. Phys.*, 1981, **14**, 4399.
110 C. T. Chen, Y. Ma and F. Sette, *Phys. Rev. A: At., Mol., Opt. Phys.*, 1989, **40**, 6737.
111 M. Domke, C. Xue, A. Puschmann, T. Mandel, E. Hudson, D. A. Shirley and G. Kaindl, *Chem. Phys. Lett.*, 1990, **173**, 122.
112 Y. Ma, C. T. Chen, G. Meigis, K. Randall and F. Sette, *Phys. Rev. A: At., Mol., Opt. Phys.*, 1991, **44**, 2848.
113 G. Remmers, M. Domke, A. Puschmann, T. Mandel, C. Xue, G. Kaindl, E. Hudson and D. A. Shirley, *Phys. Rev. A: At., Mol., Opt. Phys.*, 1992, **46**, 3935.
114 J. T. Francis, C. Enkvist, S. Lunell and A. P. Hitchcock, *Can. J. Phys.*, 1994, **72**, 879.
115 R. Püttner, I. Dominguez, T. J. Morgan, C. Cisneros, R. F. Fink, E. Rotenberg, T. Warwick, M. Domke, G. Kaindl and A. S. Schlachter, *Phys. Rev. A: At., Mol., Opt. Phys.*, 1999, **59**, 3415.
116 J. Adachi, N. Kosugi, E. Shigemasa and A. Yagishita, *Chem. Phys. Lett.*, 1999, **309**, 427.
117 P. Glans, R. E. La Villa, Y. Luo, H. Ågren and J. Nordgren, *J. Phys. B: At., Mol. Opt. Phys.*, 1994, **27**, 3399.
118 J. Nordgren, H. Ågren, L. O. Werne, C. Nordling and K. Siegbahn, *J. Phys. B: At. Mol. Phys.*, 1976, **9**, 295.
119 R. Brammer, J.-E. Rubensson, N. Wassdahl and J. Nordgren, *Phys. Scr.*, 1987, **36**, 262.
120 P. Skytt, P. Glans, K. Gunnelin, J. Guo, J. Nordgren, Y. Luo and H. Ågren, *Phys. Rev. A: At., Mol., Opt. Phys.*, 1997, **55**, 134.
121 S. Kashtanov, A. Augustsson, Y. Luo, J.-L. Guo, C. Sathe, J. E. Rubensson, H. Siegbahn, J. Nordgren and H. Ågren, *Phys. Rev. B: Condens. Matter Mater. Phys.*, 2004, **69**, 024201.